Jefferson Lab

Newport News, VA

GlueX/Hall D Calorimeter Final Design and Safety Review
February 19-20, 2008

Section 1:
Physics and Calorimeter Performance Metrics

GlueX/Hall D Calorimeter Conceptual Design Report
Section 1 of 5

1 Physics and Calorimeter Performance Metrics

We start this report on GLUEX calorimetry by discussing the physics goals of the GLUEX project – mapping the spectrum of gluonic excitations starting with exotic hybrid mesons. We show that the search for exotic mesons depends critically on detecting and measuring the four-momenta of charged particles and photons resulting from the decays of photoproduced mesons. This report focuses on the electromagnetic calorimetry needed to detect and measure those photons. It is the physics goals that determine the performance metrics of the calorimetry, including granularity, energy, position and timing resolution, and energy thresholds. Information from the calorimetry will also be used for separating protons from pions and also to provide some information on recoil neutrons. The GLUEX calorimetry consists of a cylindrical barrel (BCAL) surrounding the target and tracking chambers and a downstream planar calorimeter (FCAL).

The discussion of this introductory section will be followed by a presentation of how the performance metrics will be met in the BCAL and FCAL designs that borrow from the experience of similar calorimeters. The BCAL design uses a lead/scintillating fiber matrix similar to that used in the KLOE calorimeter [1, 2] while FCAL uses a lead glass stack similar to that used in Brookhaven experiment E852 [3, 4] and the RADPHI experiment[5, 6] at Jefferson Lab.

The requirements on acceptance and on energy, position and timing resolution are driven by the need to identify exclusive reactions in order to perform the amplitude analyses that will extract meson J^{PC} quantum numbers and on the need to be sensitive to a variety of meson decay modes. The BCAL and FCAL discussions will be followed by a presentation of GEANT-based simulations, photon reconstruction and kinematic fitting for various of the GLUEX signature reactions to assess how BCAL and FCAL, operating in the overall detector environment, will meet the GLUEX physics goals.

1.1 Physics motivation: the search for exotic mesons

1.1.1 QCD and light meson spectroscopy

The observation, nearly four decades ago, that mesons are grouped in nonets, each characterized by unique values of J^{PC} – spin (J), parity (P) and charge conjugation (C) quantum numbers – led to the development of the quark model. Within this picture, mesons are bound states of a quark (q) and antiquark ($\bar{q}$). The three light-quark flavors (*up*, *down* and *strange*) suffice to explain the spectroscopy of most – but not all – of the lighter-mass mesons (below 3 GeV/c^2) that do not explicitly carry heavy flavors (charm or beauty). Early observations yielded only those J^{PC} quantum numbers consistent with a fermion-antifermion bound state. The J^{PC} quantum numbers of a $q\bar{q}$ system with total quark spin, $\vec{S}$, and relative angular momentum, $\vec{L}$, are determined as follows: $\vec{J} = \vec{L} + \vec{S}$, $P = (-1)^{L+1}$ and $C = (-1)^{L+S}$. Thus J^{PC} quantum numbers such as 0^{--}, 0^{+-}, 1^{-+} and 2^{+-} are not allowed and are called *exotic* in this context.

Our understanding of how quarks form mesons has evolved within quantum chromodynamics (QCD) and we now expect a richer spectrum of mesons that takes into account not only the quark degrees of freedom but also the gluonic degrees of freedom. Gluonic mesons with no quarks (*glueballs*) are expected. These are bound states of pure glue and since the quantum numbers of low-lying glueballs (below 4 GeV/c^2) are not exotic, they should manifest themselves as extraneous states that cannot be accommodated within $q\bar{q}$ nonets. But their unambiguous identification is complicated by the fact that they can mix with $q\bar{q}$. Excitations of the gluonic field binding the quarks can also give rise to so-called *hybrid* mesons that can be viewed as

bound states of a quark, antiquark and valence gluon ($q\bar{q}g$). An alternative picture of hybrid mesons, one supported by lattice QCD [7], is one in which a gluonic flux tube forms between the quark and antiquark and the excitations of this flux tube lead to so-called *hybrid* mesons. Actually the idea of flux tubes, or strings connecting the quarks, originated in the early 1970's [8] to explain the observed linear dependence of the mass-squared of hadrons on spin (Regge trajectories). Conventional $q\bar{q}$ mesons arise when the flux tube is in its ground state. Hybrid mesons arise when the flux tube is excited and some hybrid mesons can have a unique signature, exotic J^{PC}, and the spectroscopy of these exotic hybrid mesons is simplified because they do not mix with conventional $q\bar{q}$ states.

The level splitting between the ground state flux tube and the first excited transverse modes is π/r, where r is the separation between the quarks, so the hybrid spectrum should lie about 1 GeV/c^2 above the ground state spectrum. While the flux-tube model [9] has all hybrid nonets degenerate in mass, from lattice gauge calculations [10], one expects the lightest $J^{PC} = 1^{-+}$ exotic hybrid to have a mass of about 1.9 GeV/c^2. In this discussion the motion of the quarks was ignored, but we know from general principles [9] that an approximation that ignores the impact of the flux tube excitation and quark motion on each other seems to work quite well. It should be noted, also, the in the large-N_c limit of QCD, exotic hybrids are expected to have narrow widths, comparable to $q\bar{q}$ states [11].

In the coming years there will be significant computational resources dedicated to understanding non-perturbative QCD including confinement using lattice techniques. The prediction of the hybrid spectrum, including decays, will be a key part of this program but experimental data will be needed to verify these calculations. The spectroscopy of exotic mesons provides a clean and attractive starting point for the study of gluonic excitations.

The GLUEX experiment is designed to collect high quality and high statistics data on the photoproduction of light mesons. As part of the program of identifying exotic hybrid mesons, these data will also be used to understand the conventional meson spectrum including the poorly understood excited vector mesons.

1.1.2 Using linearly polarized photons

There are tantalizing suggestions, mainly from experiments using beams of π mesons, that exotic hybrid mesons exist. The evidence is by no means clear cut, owing in part, to the apparently small production rates for these states in the decay channels examined. It is safe to conclude that the extensive data collected to date with π probes have not uncovered the hybrid meson spectrum. (A recent paper by E. Klempt and A. Zaitsev gives an encyclopedic and critical overview of the current experimental situation with regard to searches for glueballs, hybrids and multiquark mesons[12].) Models, like the flux-tube model, however, indicate the photon is a probe that should be particularly effective in producing exotic hybrids, but data on photoproduction of light mesons are sparse indeed.

The first excited transverse modes of the flux tube are degenerate and correspond to clockwise or counter-clockwise rotations of the flux tube about the axis joining the quark and antiquark fixed in space with $J = 1$ [9]. Linear combinations of these two modes are eigenstates of parity and lead to $J^{PC} = 1^{+-}$ and $J^{PC} = 1^{-+}$ for the excited flux tube. When these quantum numbers are combined with those of the $q\bar{q}$ with $\vec{L} = 0$ and $\vec{S} = 1$ (quark spins aligned) three of the six possible J^{PC} have exotic combinations: 0^{+-}, 1^{-+} and 2^{+-}. A photon probe is a virtual $q\bar{q}$ with quark spins aligned. In contrast when the $q\bar{q}$ have $\vec{L} = 0$ and $\vec{S} = 0$ (spins anti-aligned), the resulting quantum numbers of the hybrid meson are not exotic. Pion probes are $q\bar{q}$ with quark spins anti-aligned. If we view one outcome of the scattering process as exciting the flux tube binding the quarks in the probe, the suppression of exotic hybrids in π-induced reactions is not surprising – a spin

flip of one of the quarks is required followed by the excitation of the flux tube. In contrast the spins of the virtual quarks in the photon probe are properly aligned to lead to exotic hybrids. Phenomenological studies quantitatively support this picture predicting that the photoproduction cross-sections for exotic mesons are comparable to those for conventional mesons [13].

Determining the quantum numbers of mesons produced in the GLUEX experiment will require an amplitude analysis based on measuring the energy and momentum of their decay products. Linear polarization of the incident photon is required for a precision amplitude analysis to identify exotic quantum numbers, to understand details of the production mechanism of exotic and conventional mesons and to remove backgrounds due to conventional processes. Linear polarization will be achieved using the coherent bremsstrahlung technique.

For the GLUEX solenoid-based detector system, given the required mass reach required for mapping the spectrum of exotic hybrid mesons, a photon energy of ≈ 9 GeV is ideal. To achieve the requisite degree of linear polarization for 9 GeV photons using coherent bremsstrahlung requires a minimum electron energy of 12 GeV.

1.1.3 Expected decay modes of exotic hybrid mesons

Table 1.1 lists predicted J^{PC} exotic mesons and their decay modes. According to the flux tube model and verified by lattice QCD [14], the preferred decay modes for exotic hybrids are into $(q\bar{q})_P + (q\bar{q})_S$ mesons such as $b_1 + \pi$ or $f_1 + \pi$. Table 1.2 lists candidate exotic $J^{PC} = 1^{-+}$ state for which evidence has been claimed. The purported exotic states include decay modes into $b_1\pi$ or $f_1\pi$ as well as decay modes into $\eta\pi$ and $\eta'\pi$. The dominant branching fractions for meson states listed among the decay products are summarized in Table 1.3. Clearly, exotic meson spectroscopy requires the ability to detect and measure charged particles as well as π^0 and η mesons.

Some of the preferred or observed exotic hybrid decay modes listed in Tables 1.1 and 1.2 do not necessarily involve π^0 mesons, *e.g.* the $\rho\pi$ or $a_2\pi$ modes – these can have final states that only involve $\pi^\pm$ such as $(\rho\pi)^+ \to \pi^+\pi^+\pi^-$. But if a state decays into such an all charged π system, having the isospin partners available, such as $(\rho\pi)^+ \to \pi^+\pi^0\pi^0$ provides important isospin consistency checks of the amplitude analysis and understanding of the detector acceptance.

Exotic Meson	J^{PC}	I	G	Possible Modes
b_0	0^{+-}	1	$+$	
h_0	0^{+-}	0	$-$	$b_1\pi$
π_1	1^{-+}	1	$-$	$\rho\pi$, $b_1\pi$
η_1	1^{-+}	0	$+$	$a_2\pi$
b_2	2^{+-}	1	$+$	$a_2\pi$
h_2	2^{+-}	0	$-$	$\rho\pi$, $b_1\pi$

Table 1.1: Predicted J^{PC} exotic hybrid mesons and their expected decay modes. See Table 1.3 for decay modes of the b_1 and a_2 mesons.

Exotic Meson Candidate	Decay Mode
$\pi_1(1400)$	$\pi^-\eta$
	$\pi^0\eta$
$\pi_1(1600)$	$\rho^0\pi^-$
	$\eta'\pi^-$
$\pi_1(1600/2000)$	$b_1\pi$
	$f_1\pi$

Table 1.2: Reported $J^{PC} = 1^{-+}$ exotic hybrid mesons and their decay modes. See Table 1.3 for decay modes of the η', b_1 and f_1 mesons. Source: 2006 Review of Particle Physics [15].

Meson Decay Mode	Branching Fraction (%)
$\pi^0 \to 2\gamma$	99
$\eta \to 2\gamma$	39
$\eta \to 3\pi^0$	33
$\eta \to \pi^+\pi^-\pi^0$	23
$\omega \to \pi^+\pi^-\pi^0$	89
$\omega \to \pi^0\gamma$	9
$\eta' \to \pi^+\pi^-\eta$	45
$\eta' \to \pi^0\pi^0\eta$	21
$\eta' \to 2\gamma$	2
$b_1(1235) \to \omega\pi$	dominant
$f_1(1285) \to \pi^0\pi^0\pi^+\pi^-$	22
$f_1(1285) \to \eta\pi\pi$	52
$a_2(1320) \to 3\pi$	70
$a_2(1320) \to \eta\pi$	15

Table 1.3: Neutral or charged + neutral decay modes of several well established mesons. Source: 2006 Review of Particle Physics [15].

1.2 Detector overview

To achieve the primary physics goal of GLUEX, *i.e.* mapping out the spectrum of gluonic excitations, it is essential to detect photons with good acceptance and to measure their energies and positions with sufficient resolution. The photons of particular interest are those resulting from $\pi^0 \to \gamma\gamma$ and $\eta \to \gamma\gamma$ decays. The GLUEX detector, as shown in Figure 1.1, includes two electromagnetic calorimeters to detect and measure these photons.

The GLUEX detector is a solenoidal detector that is ideally suited for a fixed target photoproduction experiment. The solenoidal magnetic field traps low energy electromagnetic backgrounds (e^+e^- pairs), generated in the target, inside a small diameter beam hole that runs through the detector. The superconducting solenoid magnet produces a 2 T field. The photon beam is incident on a 30-cm LH_2 target that is surrounded by a cylindrical tracking chamber and a cylindrical electromagnetic calorimeter. Downstream of the target are circular planar tracking chambers and a circular planar electromagnetic calorimeter.
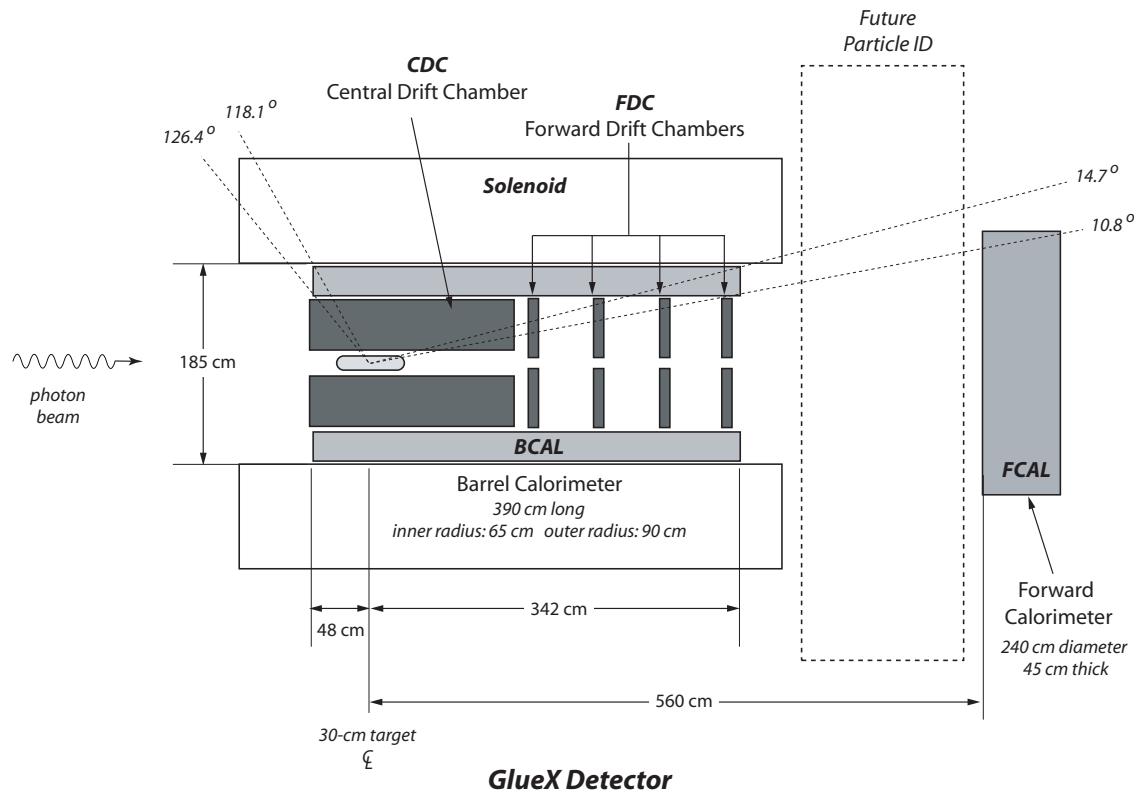

Figure 1.1: Schematic of the GLUEX Detector. The superconducting solenoid magnet produces a 2 T field. The photon beam is incident on a 30-cm LH_2 target that is surrounded by a cylindrical tracking chamber (CDC) and a cylindrical electromagnetic calorimeter (BCAL). Downstream of the target are circular planar tracking chambers (FDC) and a circular planar electromagnetic calorimeter (FCAL). The dimensions of BCAL and FCAL are shown. The detector has cylindrical symmetry about the beam direction. The dashed lines at angles (with respect to the beam direction) $10.8°$ through $126.4°$ will be referenced in the text.

1.3   Information from existing photoproduction data

There is little data on meson photoproduction in the GLUEX energy regime ($E_\gamma \approx 7 - 9$ GeV). Almost all of what is known comes from bubble chamber measurements at SLAC [16, 17, 18, 19, 20, 21]. These experiments were among the first exploratory studies of the photoproduction of meson and baryon resonances at these energies, and although they suffer from low-statistics, they have good acceptance, except for events with multiple neutrals. Exclusive reactions leading to final states with charged particles and a single neutron or π^0 can be identified by kinematic fitting. Table 1.4 summarizes the photoproduction cross sections for various charged particle topologies, with and without neutrals, at $E_\gamma = 9.3$ GeV [16]. Final states with single or multi-neutral particles (π^0, η or n) account for about 82% of the total cross section. About 13% of the total cross section is due to final states with charged particles and a single π^0. So for about 70% of the total photoproduction cross section, from $E_\gamma \approx 7$ to ≈ 12 GeV, we have essentially no information. Extrapolating from what is known from the final states that have been identified and studied, the bulk of the unknown processes are expected to involve final states with combinations of π^0 and η mesons. The discovery potential of GLUEX rests on being able to detect π^0 and η mesons.

Topology	σ (μb)	% of σ with neutrals
1-prong	8.5 ± 1.1	100
3-prong	64.1 ± 1.5	76 ± 3
5-prong	34.2 ± 0.9	86 ± 4
7-prong	6.8 ± 0.3	86 ± 6
9-prong	0.61 ± 0.08	87 ± 21
With visible strange decay	9.8 ± 0.4	-
Total	124.0 ± 2.5	82 ± 4

Table 1.4: Topological photoproduction cross sections for γp interactions at 9.3 GeV from Reference [16]. Also shown are the percent of the cross section with neutral particles for each topology.

Baryon resonance decays: Photoproduction of meson resonances in the GLUEX energy regime typically result in the meson being produced at small absolute values of the momentum transfer squared $|t|$ between incoming photon and outgoing meson – or equivalently between target proton and recoil nucleon or baryon resonance. The produced meson, as well as its decay products (depending on the particle multiplicity and relative mother-daughter masses), move in the forward direction whereas the recoil baryon moves at large angles $\gtrsim 45°$ with respect to the beam direction. If the recoil baryon is a baryon resonance, such as a Δ or N^*, decays involving π^0 are possible. It will be important to identify the soft, wide-angle π^0 mesons from such decays since the amplitude analysis depends on starting with a known exclusive reaction.

1.4 π^0 and η Kinematics

1.4.1   Overview

Here we review how the decay photons from photoproduced meson and baryon resonances populate LAB energy-angle space at GLUEX energies. Please refer to Figure 1.1 that shows a schematic of the GLUEX detector. Note the dotted lines showing angles at 10.8° and 126.4°. Photons whose angles lie within this range will be detected and measured by BCAL. Photons with angles between 1° and 10.8° will be detected and measured by FCAL. Photons whose angles are greater than 126.4° or less than 1° will be undetected.

1.4.2 Studies using PYTHIA

As noted above, much is unknown about photoproduction at GLUEX energies leading to multi-neutral final states. To estimate photon yields we used the Monte Carlo program PYTHIA [22] that was written to generate high energy physics events produced in a wide variety of initial states, including fixed target photoproduction. The program is based on a combination of analytical results and QCD-based models of particle interactions. PYTHIA was designed to allow for tuning parameters to suit the particular situation – for example, photoproduction at 9 GeV. The output of the simulations were compared [23] to published data, in particular, reference [16]. Comparison of cross section estimates for charged particle topologies and several reactions in the 3-prong and 5-prong, which accounts for 80% of the total cross section, are shown in Tables 1.5 and 1.6. The vector mesons ρ, ω and ϕ appear in the 3-prong sample in the $\pi^+\pi^- p$, $\pi^+\pi^-\pi^0 p$ and $K^+K^- p$ final states respectively. The distribution in $|t|$ for PYTHIA events agrees with published data for specific reactions. PYTHIA accounts for Δ resonance production. In the $\pi^+\pi^- K^+ K^- p$ state, the $K^*(890)$ is present.

Topology	PYTHIA Estimates (μb)	Data (μb)
1-prong	8.8 ± 0.02	8.5 ± 1.1
3-prong	63.5 ± 0.09	64.1 ± 1.5
5-prong	42.7 ± 0.2	34.2 ± 0.9
7-prong	7.3 ± 0.1	6.8 ± 0.3
9-prong	0.3 ± 0.1	0.61 ± 0.08

Table 1.5: Topological Photoproduction Cross Sections at 9 GeV from PYTHIA and from bubble chamber data [16]. The PYTHIA cross section estimates have been tuned to a total photoproduction cross section of 124 μb. The errors on the PYTHIA estimates are statistical.

Reaction	PYTHIA Estimates (μb)	Data (μb)
	$\gamma p \to 3$ prongs	
$\gamma p \to p\pi^+\pi^-$	13.6 ± 0.13	14.7 ± 0.6
$\gamma p \to pK^+K^-$	0.41 ± 0.02	0.58 ± 0.05
$\gamma p \to p\bar{p}p$	0.04 ± 0.01	0.09 ± 0.02
$\gamma p \to p\pi^+\pi^-\pi^0$	5.8 ± 0.1	7.5 ± 0.8
$\gamma p \to n2\pi^+\pi^-$	1.4 ± 0.04	3.2 ± 0.7
With multi-neutrals	42.3 ± 0.3	38.0 ± 1.9
	$\gamma p \to 5$ prongs	
$\gamma p \to p2\pi^+2\pi^-$	2.9 ± 0.06	4.1 ± 0.2
$\gamma p \to pK^+K^-\pi^+\pi^-$	0.51 ± 0.03	0.46 ± 0.08
$\gamma p \to p2\pi^+2\pi^-\pi^0$	8.12 ± 0.1	6.7 ± 1.0
$\gamma p \to n3\pi^+2\pi^-$	$0.8 \pm .3$	1.8 ± 1.9
With multi-neutrals	30.4 ± 0.2	21.1 ± 1.7

Table 1.6: Photoproduction reaction cross sections at 9 GeV from PYTHIA and from bubble chamber data [16]. The PYTHIA cross section estimates have been tuned to a total photoproduction cross section of 124 μb. The errors on the PYTHIA estimates are statistical.

Photon distributions in energy and angle: We now use this version of PYTHIA tuned to provide reasonable agreement with published data, to provide estimates of the multiplicity of photons in the GLUEX calorimeters along with their energies and angles. Figure 1.2 shows photon information for 1M PYTHIA events. About 78% of the events have at least one photon leading to a 3.2M photon sample. The photon multiplicity

is shown in Figure 1.2(a) The correlation of photon energy with angle is shown for all photons in BCAL (Figure 1.2(b)), in FCAL (Figure 1.2(c)) and for photons with angles greater than 126° (Figure 1.2(d)). The percentage of all photons entering FCAL is 27.3%, entering BCAL is 70.5%, with angles greater than 126° is 1.7% and entering the beam hole in FCAL (defined by angles less than 1°) is 0.5%. So BCAL and FCAL together will be illuminated by about 98% of all photons with BCAL having about 2.5 times more photons than FCAL. The implications of not detecting the 1.7% of photons that have angles greater than 126° will be discussed below.

Energy threshold: An important parameter for either calorimeter is the energy threshold. Table 1.7 shows the fraction (in percent) of events with more than one photon in a calorimeter for which the minimum energy in the event is less than the threshold energy. These are percentages obtained by averaging over all topologies (charged and neutral particles). As will be seen below, for some signature reactions in GLUEX involving multiple photons and charged particles, the overall event acceptance will depend critically on the minimum energy at which a photon can be reconstructed.
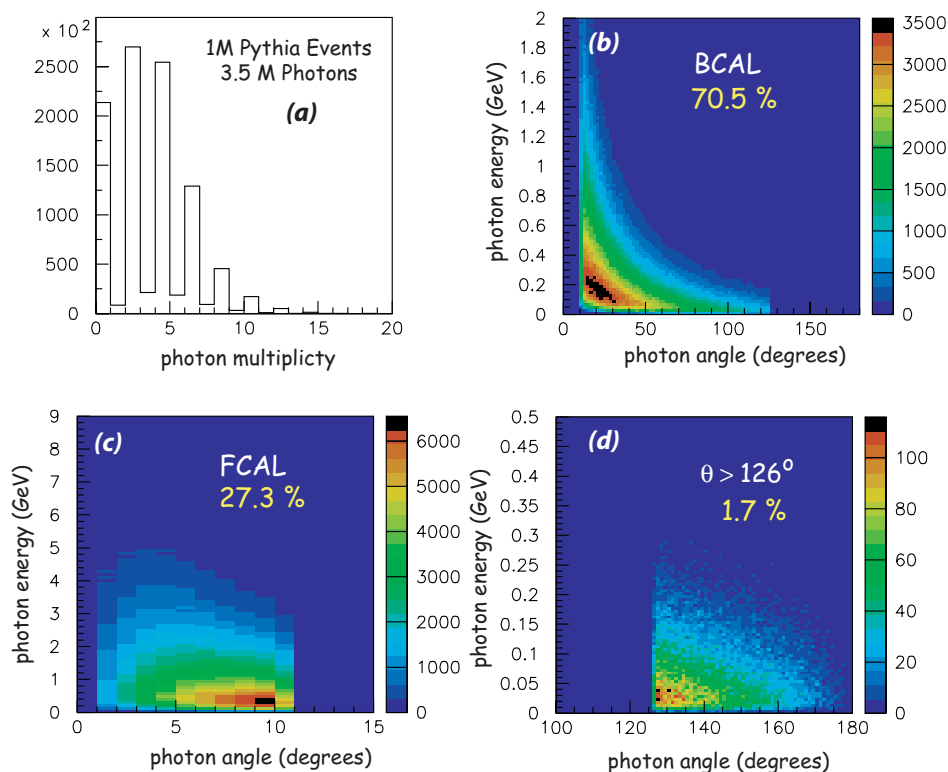

Figure 1.2: (a) Photon multiplicity for 1M PYTHIA events. About 78% of the events have at least one photon leading to a 3.2M photon sample. The correlation of photon energy with angle is shown for photons in (b) BCAL, (c) FCAL and (d) for photons with angles greater than 126°. Note that the plot axes have different scales.

BCAL granularity: The plots of Figure 1.3 address the issue of the granularity needed for BCAL. Distributions for (a) photon multiplicity in BCAL for events with one or more photons in BCAL; (b) separation of photons in azimuthal angle for photons in BCAL (multiple entries per event); and (c) minimum azimuthal angle separation in an event are shown. Also shown is the correlation of azimuthal separation (all di-photon

Energy Threshold E_{thr} (MeV)	BCAL: % with $E_{min} < E_{thr}$	FCAL: % with $E_{min} < E_{thr}$
20	2	0
40	5	0.1
50	8	0.2
100	17	1.9
150	25	4.8

Table 1.7: Fraction (in percent) of events with more than one photon in a calorimeter for which the minimum energy in an event is less than the threshold energy.

combinations in an event) with photon multiplicity. As will be described below (in the BCAL section) the BCAL readout cell size is approximately 2×2 cm^2. The in depth (along the radius) the segmentation is exactly 2 cm and along the azimuth the width varies with depth to correspond to an azimuthal segmentation of $1.875°$. This segmentation is for the first 12 cm in depth but it accounts for providing the bulk of information needed for photon reconstruction. Also, as will be discussed below, the segmentation for the remaining depth has a coarser segmentation. This cell size is a good match to the BCAL Molière radius (3.6 cm). Approximately 6% of events with two or more photons in BCAL have a photon pair with an azimuthal angular separation less than $2°$.

FCAL granularity: The plots of Figure 1.4 address the issue of the granularity needed for FCAL. Distributions for (a) photon multiplicity in FCAL for events with one or more photons in FCAL; (b) photon distance from center of FCAL in the plane of FCAL; and (c) photon separation in the plane of FCAL (multiple entries per event) are displayed. Also shown is the (d) (x,y) pattern of photon hits on the plane of FCAL.

The specific design of FCAL will be discussed in more detail below, but for now we note that the design follows the granularity used in E852 [3, 4] and RADPHI [5, 6] based on glass blocks with transverse dimensions of 4×4 cm^3. These dimensions are a good match to the Molière radius (4.3 cm) of the lead glass that will be used in FCAL. These PYTHIA simulations show that the percentage of all events with two or more photons in FCAL, 0.7% of these events have a minimum di-photon separation of 8 cm or less. The maximum energy π^0 (E_π^{max}) expected for GLUEX is 9 GeV for nominal running with polarized photons and 12 GeV for photon running near the electron endpoint energy. This corresponds to a minimum di-photon separation of 16 and 13 cm for the two energies, using $\Delta r = 2m_\pi L_{FCAL}/E_\pi^{max}$ with $L_{FCAL} = 560$ cm (see Figure 1.1).

1.4.3 A signature reaction: $\gamma p \to \eta \pi^0 p$

We now turn to one of the signature reactions for GLUEX, the reaction $\gamma p \to \eta \pi^0 p$. This reaction is of particular interest for exotic hybrid searches since the $\eta \pi^0$ has well-defined charge conjugation quantum number ($C = +$) and if the η and π^0 resonate in a $P - wave$ then the resonance has exotic $J^{PC} = 1^{-+}$. For events with uniform $\eta \pi^0$ masses between 1.0 and 2.0 GeV/c^2, uniform in decay angles, and produced with a $e^{-5 \cdot |t|}$ distribution, the photons populate the calorimeters, the beam hole in FCAL and the angular region $> 126°$ as shown in Table 1.8. For completeness we include the photon population for PYTHIA events as well as for the recoil baryon resonance production $\gamma p \to X\Delta \to X\pi^0 N$. The latter reaction will be discussed in more detail below.
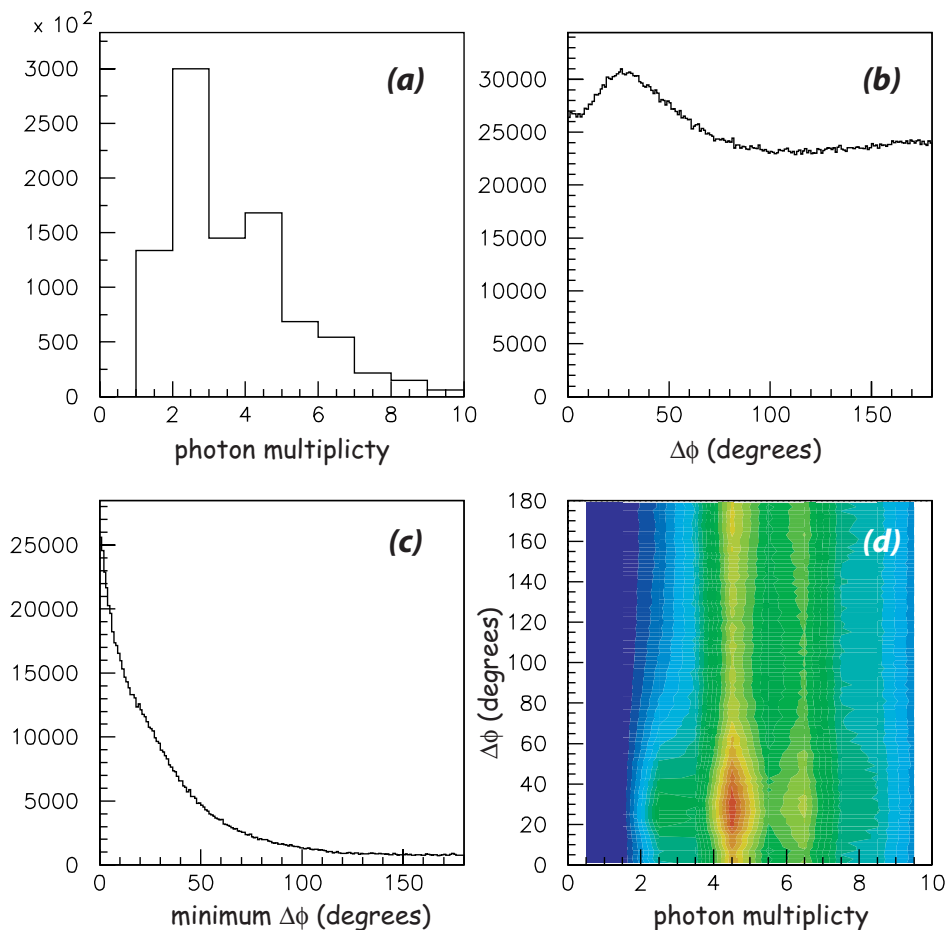
Figure 1.3: Photons in BCAL: distributions in (a) photon multiplicity in BCAL for events with one or more photons in BCAL; (b) separation of photons in azimuthal angle for photons in BCAL (multiple entries per event); (c) minimum azimuthal angle separation in an event; (d) correlation of azimuthal separation (all di-photon combinations in an event) with photon multiplicity.

Table 1.9 shows the fraction of accepted (no photons in beam hole or with angles $> 126°$) events that have both photons from the η or π^0 in FCAL or BCAL or shared between FCAL and BCAL.

Figure 1.5 has information about the photons hitting BCAL. The variable z is the distance along the inner surface of BCAL starting from the upstream end at $z = 17$ cm and ending at the downstream end at $z = 407$ cm. The 30-cm target center is at $z = 65$ cm. The histogram is the distribution of the photons along z (use the left vertical scale) while the dashed curve (use the right vertical scale) is the integral fraction of photons in percent. For example, 30% of the BCAL photons hit between $z = 17$ cm and $z = 212$ cm, the upstream half of BCAL. The other curves also use the right vertical scale. The green curve is the number of BCAL radiation lengths intercepted by the photon trajectory assuming a 1.45 cm radiation length for the Pb/SciFi matrix. The cusp at $z = 312$ cm corresponds to a photon angle of 14.7° where the number of radiation lengths is 68. As the photon angle changes from 10.8° to 14.7° (see Figure 1.1), the number of radiation lengths intercepted by the photon trajectory increases from 0 to 68. In this angular region the photon trajectory exits out the downstream end of BCAL. How well these photons can be constructed, using GEANT-based simulations and photon reconstruction software, will be discussed later. The cusp at
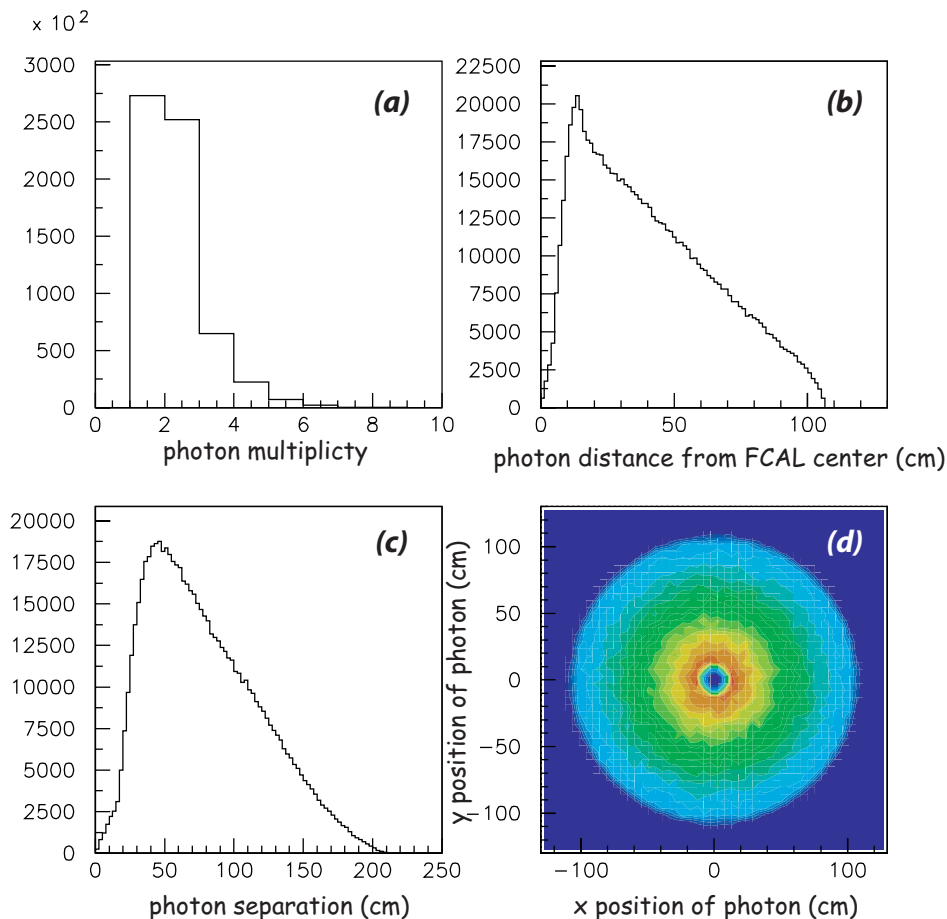
Figure 1.4: Photons in FCAL: distributions in (a) photon multiplicity in FCAL for events with one or more photons in FCAL; (b) photon distance from center of FCAL in the plane of FCAL; (c) photon separation in the plane of FCAL (multiple entries per event); and (d) (x,y) pattern of photon hits on the plane of FCAL.

$z = 30$ cm corresponds to a photon angle of $118.1°$. The minimum of the green curve is at $z = 65$ cm or at $90°$ corresponding to 17 radiation lengths (the module is 22.5 cm thick). The blue curve shows the photon angle as a function of z.

1.4.4 Amplitude analysis and understanding of acceptance

As seen in Figure 1.5, the angular region between $10.8°$ and $14.7°$ (see Figure 1.1) has a significant population of photons for events of the reaction $\gamma p \rightarrow Xp \rightarrow \eta\pi^0 p$. In this region there was a fair amount of material due to cabling associated with the FDC drift chambers in the original design, but recent changes have resulted in a significant reduction of material. The impact of remaining FDC material on photon reconstruction is currently under study. How well one understands the reconstruction efficiency in this region is critical for the amplitude analysis. To illustrate this, we generate events with a uniform population of decay angles in the X rest frame. A frame that is often chosen is the Gottfried-Jackson frame where the polar angle, θ_{GJ}, is the angle between the momentum vector of one of the decay products (the η in our case) and the momentum vector of the beam, all in the X rest frame. A uniform decay angular distribution corresponds

Element	Percent of all photons PYTHIA Events	Percent of all photons $\eta\pi^0$ Events	Percent of all photons $X\Delta$ Events
Angles > 126°	1.7	0.20	7.8
BCAL	70.5	45.68	89.8
FCAL	27.3	53.15	2.4
Hole in FCAL	0.5	0.97	0

Table 1.8: Fraction of all photons populating the GLUEX calorimeters, the angular region > 126° and the beam hole in FCAL for PYTHIA events and $\eta\pi^0$ events.

Element	η	π^0
Both photons in FCAL	27%	46%
Both photons in BCAL	20%	35%
Photons in FCAL and BCAL	53%	19%

Table 1.9: Fraction of accepted $\eta\pi^0$ events that have photons from either the η or π^0 both in BCAL or FCAL or shared.
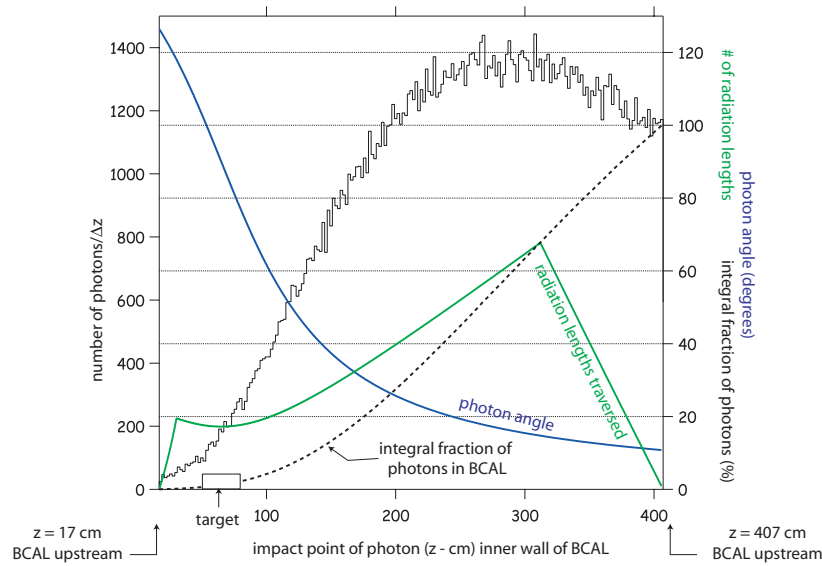
Figure 1.5: Histogram: Distribution of photons from the $\gamma p \rightarrow \eta\pi^0 p$ reaction along the inner wall of BCAL. The upstream end of BCAL is at $z = 17$ cm and the downstream end at $z = 407$ cm. Use the left vertical scale for the histogram. The three curves (all as a function of z) use the right vertical scale. The black dashed curve is the integral fraction of photons in BCAL in percent. The blue curve is the photon angle in degrees measured with respect to the beam (or with respect to the inner surface of BCAL). The green curve is the number of radiation lengths traversed by a photon.

to a distribution flat in $\cos\theta_{GJ}$. The amplitude analysis fits the observed distribution in $\cos\theta_{GJ}$ to a sum of various waves corresponding to the angular momentum L between the η and π^0 and its projection M along the $z-$axis.

In Figure 1.6 we show the effect on the $\cos\theta_{GJ}$ distribution if we eliminate $\eta\pi^0$ events if one of the four photons from the event enters an angular region defined by the LAB angle θ. For distribution (I) no requirement

was imposed. For distribution (II) the angular cut imposed extends from $\theta = 10.8°$ to $\theta = 11.7°$. For distributions (III) through (V), the lower limit remained the same while the upper limit was increased in $1°$ increments, up to $\theta = 14.7°$ for distribution (V). Also shown are the percentage of events that survive the various angular cuts along with the forward-backward asymmetry defined as $(F - B/(F + B))$ where F is the number of events with $\cos\theta_{GJ} > 0$ and B is the number of events with $\cos\theta_{GJ} < 0$. The imposition of the angular cut impacts the acceptance and sculpts the observed angular distribution. As noted above, if the $\eta\pi^0$ resonates in a P-wave ($L = 1$) the resonance has exotic quantum numbers. There are resonances with $L = 0$ and $L = 2$ that decay into $\eta\pi^0$ and an even-wave odd-wave interference will lead to a forward-backward asymmetry in the $\cos\theta_{GJ}$ distribution. So a poorly understood acceptance in the critical angular region between BCAL and FCAL can lead to false amplitude analysis conclusions.
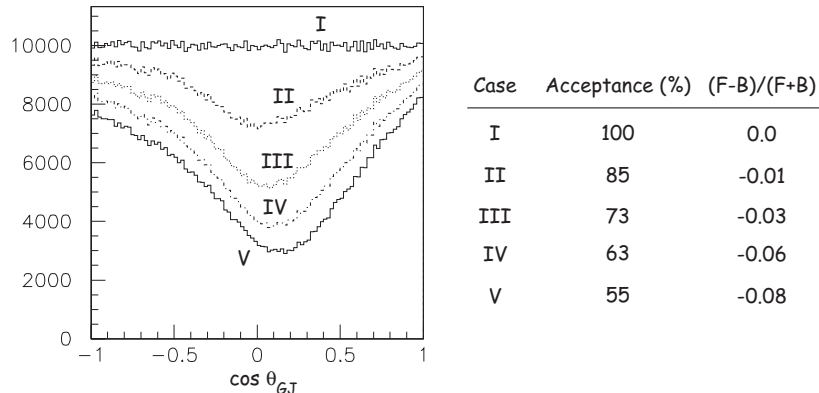
Case	Acceptance (%)	(F-B)/(F+B)
I	100	0.0
II	85	-0.01
III	73	-0.03
IV	63	-0.06
V	55	-0.08

Figure 1.6: The distribution in $\cos\theta_{GJ}$ for $\gamma p \to Xp \to \eta\pi^0 p$ events. For distribution (I) no cuts are imposed. For distributions (II) through (V), events are eliminated if one of the four photons enters various angular ranges as defined in the text. The corresponding acceptances and forward-backward asymmetries are also given.

1.4.5 Another signature reaction: $\gamma p \to b_1(1235)\pi p$

An important parameter for BCAL is the energy of the lowest energy photon that can be reconstructed. To understand the challenge we look at $\gamma p \to b_1^+ \pi^0 n$ where the intermediate final state is $\omega\pi^+\pi^0$ and the final state is $\pi^+\pi^+\pi^-\pi^0\pi^0 p$. In this note we look at the kinematics of a 2 GeV/c^2 state decaying into $b_1\pi$. The incident photon energy is assumed to be 9 GeV. This is one of our signature reactions for exotic hybrid searches and yields four photons.

The plot of Figure 1.7(a) shows the energy spectrum of the lowest energy photon in the event. The plot of Figure 1.7(b) shows the fractional running integral, so, for example, 25% of the events have a photon with energy less than 80 MeV. The scatterplot of Figure 1.8 shows the energy versus angle for the lowest energy photon in the event for $\gamma p \to b_1^+ \pi^0 n$. This scatterplot shows the challenge for this lowest energy photon reconstruction. Most of the low energy photons occur near the edge of BCAL where reconstruction is a challenge due to presence of material at that location.
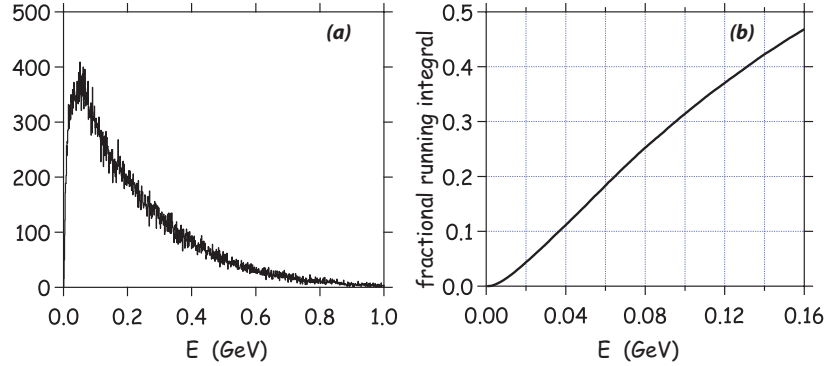
Figure 1.7: Left: Spectrum of lowest energy photon in a $\gamma p \to b_1^+ \pi^0 n$ event; Right: Fractional running integral for the plot to the left.

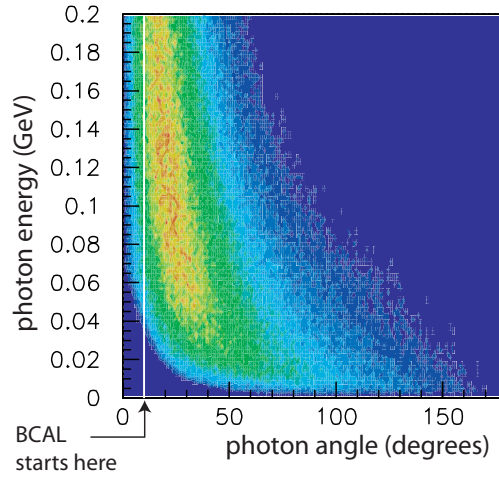Figure 1.8: Energy versus angle for the lowest energy photon in the event for $\gamma p \to b_1^+ \pi^0 n$.

1.5 Photon coverage at large angles

As noted in Figure 1.1, there is no photon detection for photons with angles $> 126°$ and from Table 1.8 we see that the percentage of all photons for PYTHIA events and for $\eta \pi^0$ events that populate this angular is small. The class of photoproduction reactions that populate this angular region with photon are reactions resulting in the production of a forward meson (X) and a recoil excited baryon decaying into $\pi^0 p$ or $\pi^0 n$. Since the application of the amplitude analysis depends on identification of exclusive final states, it will be important to identify such reactions by explicitly measuring the decay products of the baryon resonance or to veto events offline that have a extraneous π^0 or photons too low in energy to be identified kinematically given the limitations on resolution in missing mass.

To understand the effect of the presence of baryon resonances we generated $\gamma p \to X\Delta$ events where X is a resonance of mass uniformly distributed between 1.0 and 2.0 GeV/c^2 and produced with a distribution in momentum transfer squared (t) given by $e^{-5 \cdot |t|}$. The Δ mass and width are 1.236 and 0.15 GeV/c^2 respectively and the decay mode is $\pi^0 N$. The kinematics of the recoil baryon is determined by the value of $|t|$ and is independent of M_X expect for the dependence of $|t|_{min}$ on M_X. The percent of all photons

generated that populate various angular regions is summarized in Table 1.8. The percentage of photons with angles $> 126°$ is relatively large but these events can be tagged for elimination by using information from FCAL and BCAL, but primarily the latter. For the sample generated, 80% of the events have both photons from the π^0 (the Δ decay product) in BCAL and 85% have both photons in either FCAL or BCAL or shared between the two. Only 0.3% of the events have no photons in either FCAL or BCAL so effectively more than 99% of the baryon resonance events can either be measured or tagged.

Extending the upstream end of BCAL by 30 cm would increase the backward angle coverage to $140°$ and would recover about 50% of the backwards-going photons that are now missed. Extending to $140°$ would recover 70% of the photons missed with the current configuration but would require adding and additional 67 cm to the calorimeter. The deterioration in BCAL performance by such modifications would not be justified by this additional photon coverage.

How large are these baryon resonance cross sections? The cross section measurements near GLUEX energies show significant Δ^{++} production in the 3-prong and 5-prong topologies but little Δ^+ or Δ^0 production. For example, in the 3-prong topology, the cross sections for $\rho^-\Delta^{++}$, $\rho^0\Delta^+$ and $\rho^+\Delta^0$ are 1.1 ± 0.2 μb, 0.3 ± 0.2 μb and 0.2 ± 0.2 μb respectively. The cross sections for $n\rho^0\pi^+$ and $\Delta^-\pi^+\pi^+$ are 2.0 ± 0.6 μb and 0.2 ± 0.2 μb respectively [24]. In the 5-prong channel with a single π^0, reactions with a Δ^{++} account for nearly 75% of that channel but no reactions with Δ^+ are quoted. Although measurements are based on low statistics, there appears to be little Δ^+ or Δ^0 production.

1.6 Photon energy and position resolutions

The ability to efficiently reconstruct π^0 and η mesons is what drives the requirements on photon energy and position resolutions that in turn determine the mass resolutions of the π^0 and η masses. To understand this interplay we generated events corresponding to the reaction $\gamma p \rightarrow \eta\pi^0 p \rightarrow 4\gamma p$ at $E_\gamma = 9$ GeV, with $\eta\pi^0$ mass distribution uniform in mass from 1 to 2 GeV/c^2 and uniform in angles with $t-$dependent production of $e^{-5\cdot|t|}$.

Energy resolution: The photon energies were smeared to follow the following resolution function[1]:

$$\frac{\sigma_E}{E} = \frac{a}{\sqrt{E(\text{GeV})}} \oplus b \tag{1.1}$$

For BCAL we use 0.054 GeV$^{-1/2}$ and $b = 0.01$, from GEANT simulations [25], which are also consistent with resolutions obtained with the KLOE calorimeter [1, 2] and with the beam tests of a BCAL 4-m module prototype [26]. The GEANT simulations, KLOE experience, and BCAL prototype tests will be described in more detail below. For FCAL we use 0.073 GeV$^{-1/2}$ and $b = 0.036$, as obtained for the RADPHI calorimeter [5, 6].

---

[1]From here on, in this Section and following Sections, we will assume the same form for the energy resolution and the constants a and b, which represent the *statistical* and *floor* contributions respectively, will be given either as a percent or fraction assuming that the energy E is given in units of GeV.

Position resolution: For BCAL, we use the following resolution in $R\phi$ where R is the BCAL inner radius (65 cm) and ϕ is the azimuthal angle:

$$\delta(R\phi) = \frac{5 \text{ mm}}{\sqrt{\text{E(GeV)}}} \tag{1.2}$$

The above assumption is consistent with results of BCAL simulations [25] and with the proposed inner 2×2 cm^2 readout scheme for the ends of the BCAL modules. The polar angle, θ, resolution is assumed to be driven by the resolution in z along the BCAL fiber which in turn is driven by the resolution in time difference between the two ends of a BCAL module. We assume the timing resolution is given by:

$$\sigma_t(\text{ps}) = \frac{54}{\sqrt{\text{E(GeV)}}} \oplus 50 \tag{1.3}$$

and the resolution in z is given by $dz = \sigma_t \cdot v_{eff}/2$ where v_{eff} is the effective velocity of light in the fibers that takes into account the index of refraction and bounces ($v_{eff} = 0.53c$). With this:

$$\sigma_\theta = \frac{R}{R^2 + z^2} dz \tag{1.4}$$

Figure 1.9 shows the dependence of σ_θ as a function of θ for various photon energies.
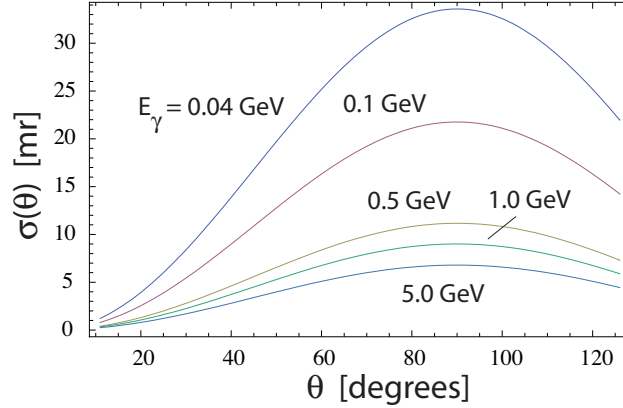

Figure 1.9: BCAL polar angular resolution as a function of angle for photon energies of 0.04, 0.1, 0.5 and 1.0 GeV.

For FCAL we assume a position resolution in the plane of FCAL to be [5].

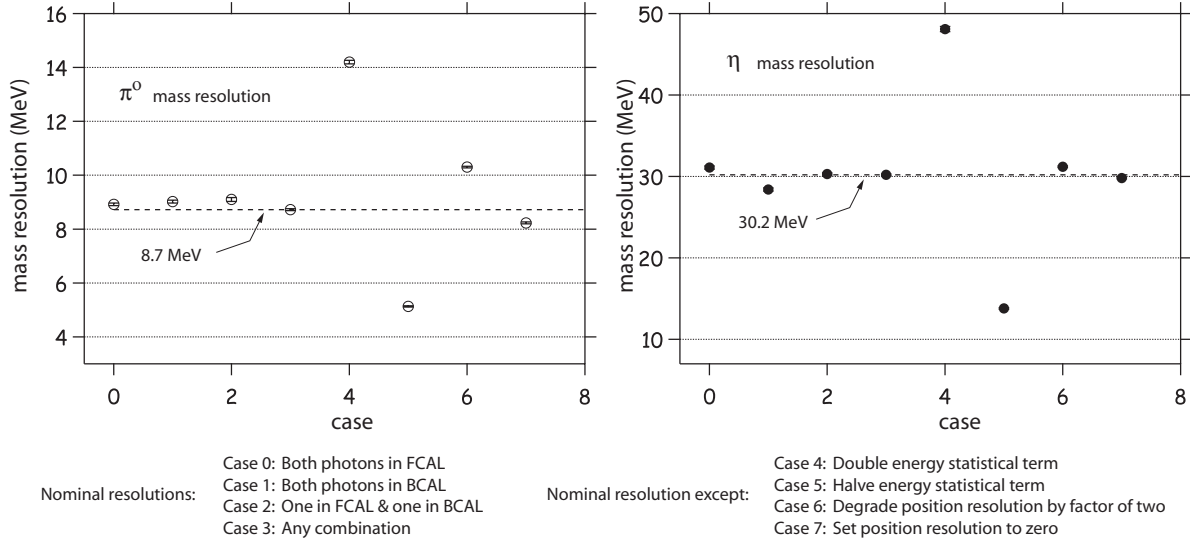$$\sigma_r = \frac{6.4 \text{ mm}}{\sqrt{\text{E(GeV)}}} \tag{1.5}$$

Figure 1.10: The π^0 and η mass resolutions obtained under different assumptions for energy and position resolutions in FCAL and BCAL.

Mass resolutions: Given these assumptions as defining our *nominal* resolutions, we smear the photon energies and positions and compute the di-photon masses for the photons originating from the η decay and from the π^0. The resulting distributions, assuming nominal resolutions, are fit to a Gaussian and the widths obtained from these fits are plotted in Figure 1.10. Several cases are considered: (0) when both photons from the η or π^0 are in FCAL; (1) when both photons are in BCAL; (2) when one photon is in BCAL and the other in FCAL; and (3) any combination of FCAL/BCAL. We also considered, for any combination, degrading or improving the nominal resolution such (4) doubling the statistical term in the energy resolution; (5) halving the statistical term in the energy resolution; (6) degrading the position resolution by a factor of two and (7) assuming perfect position determination. The mass resolutions for the η and π^0 are 30.2 MeV/c^2 and 8.7 MeV/c^2 respectively. By comparison the η and π^0 widths were measured as 30.8 ± 0.5 MeV/c^2 and 12.1 ± 0.1 MeV/c^2 respectively in E852 for the reaction $\pi^- p \to \eta \pi^0 n$ [27]. The mass resolution is primarily driven by the energy resolution and the mass resolution of the π^0 is more sensitive to the position resolution compared to the η.

Figure 1.11 shows the diphoton mass for the $\eta \pi^0$ reaction with six entries per event after resolution smearing assuming nominal resolutions and degrading and improving the energy resolution by a factor of two. Also shown are the results of fitting the spectrum near the η mass region to a sum of a Gaussian and linear background. Both signal and combinatoric background are integrated over $\pm 2\sigma$ to obtain an estimate of signal (S) over combinatoric background (N). In this study the combinatoric background in the four-photon sample comes from $\eta \pi^0$ events. The four-photon sample will also be populated by $\pi^0 \pi^0$ events which will increase the combinatoric background depending on the relative cross-sections for these two final states. Kinematic fitting can be used to eliminate the $\pi^0 \pi^0$ events from the four photon sample. This technique was used in the E852 experiment to study $\eta \pi^0$ final state [28] which has a cross-section about an order of magnitude lower than for the $\pi^0 \pi^0$ final state in π-induced interactions. Another source feeding the four-photon sample will be final states with more than four photons where one of the photons is undetected or final states with fewer than four photons but with spurious additional photons either resulting from interactions in detector material or due to an artifact of the reconstruction software. These issues will be discussed in the section on studies with full detector simulations and reconstruction.
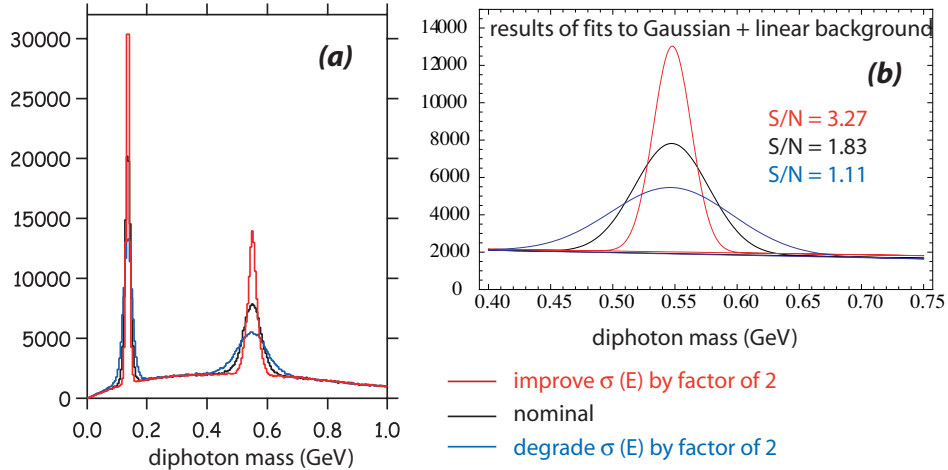
Figure 1.11: (a) The diphoton mass for the $\eta\pi^0$ reaction after resolution smearing using nominal resolutions (black), improving σ_E by a factor of two (red) and degrading σ_E by a factor of two (blue). There are six combinations per event. (b) Results of fitting the η mass region with a Gaussian and linear background. The background and signal were integrated over $\pm 2\sigma$ to obtain signal over noise S/N for the three resolution assumptions.

1.7 Mass resolutions involving charged particles and photons

To compare the contributions of charged particle resolution and photon resolutions to narrow width particles, as in the decays $\eta \to \pi^+\pi^-\pi^0$, $\omega \to \pi^+\pi^-\pi^0$ and $\phi \to \pi^+\pi^-\pi^0$ we studied the reaction $\gamma p \to \phi p$. For this study, the distribution in $|t|$ followed $e^{-|t|/2}$ to provide a mix of charged particle momenta that would include more lower momentum particles. The ϕ was generated with a mass and width of 1020 and 4 MeV/c^2 respectively. The photon energies and angles were smeared according to the nominal resolutions discussed above. The charged particle four vectors (for the $\pi^\pm$) were smeared to follow the momentum error and angular error plots generated in a study of track finding in GLUEX [29]. The plots shown in the referenced study were fit to analytical forms. These plots were generated before the material associated with the CDC and FDC tracking chambers was reduced so in what follows we consider the nominal charged particle resolutions and resolutions improved by a factor of two. The effect of the resolution smearing on the observed width of the ϕ is shown in Table 1.10. The distribution in the square of the missing mass recoiling against the ϕ is shown in Figure 1.12 under various assumptions of four-vector smearing.

Condition	Nominal errors for $\pi^\pm$	Nominal errors/2 for $\pi^\pm$
Photon smearing only	14.8 ± 0.1 MeV/c^2	14.8 ± 0.1 MeV/c^2
Charged particle smearing only	16.7 ± 0.1 MeV/c^2	11.1 ± 0.1 MeV/c^2
Both smeared	22.2 ± 0.2 MeV/c^2	17.6 ± 0.1 MeV/c^2

Table 1.10: Observed width for the ϕ, generated with a width of 4 MeV/c^2, after four-vector smearing.

1.8 Time of flight information

As noted above, information about the time difference between the two ends of the BCAL module photosensor readout provides the impact point (z-position) of photons striking the inner surface of BCAL. The average
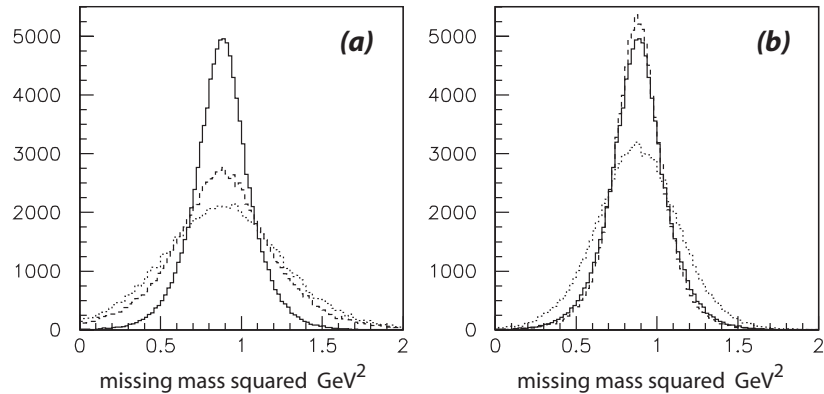
Figure 1.12: Missing mass squared recoiling off the ϕ for the reaction $\gamma p \rightarrow \phi p$ with photon smearing only (solid histogram), charged particle smearing only (dashed) and both (light dashed) for nominal charged particle smearing (a) and smearing reduced by a factor of two (b).

time, or mean time, of the two ends can be used to provide time of flight information that may be used for particle identification. The time difference is relevant and crucial for determining the four-vector information for photons.

The mean time information could, in principle, be used for particle identification for hadrons, in particular in providing π/K or π/p separation. As will be discussed in what follows, the mean time resolution obtained from cosmic ray (minimum ionizing particle) measurements with a 4 m module, is approximately 500 ps. This time resolution is inadequate for π/K separation but can be used for π/p separation.

We generated events to simulate the reaction $\gamma p \rightarrow \pi^+ \pi^- \pi^0 n$ where the 3π result from the decay $a_2(1320) \rightarrow \rho\pi$ or $\pi_2(1320) \rightarrow f_2\pi$ with a $e^{-5 \cdot |t|}$. The charged particles were tracked through a uniform magnetic field and for $\pi^\pm$ reaching BCAL the π/K difference was computed. The time difference distribution is shown in Figure 1.13(a). CLearly, a 500 ps mean-time resolution does not allow for π/K separation. For protons reaching BCAL, we compute the π/p time difference divided by 500 ps. The resulting distribution is shown in Figure 1.13(b). About 77% of the events where the proton track has sufficient transverse momentum to reach BCAL have a $(t_p - t_\pi)/\sigma_t > 4$.

1.9 Expectations for amplitude analyses

The ultimate goal of the GLUEX experiment is to identify exotic mesons by an amplitude analysis of exclusive final states. The sensitivity of the amplitude analysis, *i.e.* how small a signal can be detected, depends on having sufficient statistics and how well systematics, both from the experiment and from the analysis, are controlled. GLUEX collaborators have recently been awarded an NSF grant to develop tools for understanding the phenomenological systematics inherent in an amplitude analysis. To estimate the sensitivity we expect from GLUEX requires a full simulation of the detector response to real and background events, charged particle and photon reconstruction, kinematic fitting to identify exclusive final states and finally the actual amplitude analysis. Work is in progress and the last section of this report summarizes results from the first steps along this program.

In the meantime, we can turn to results of analyses from experiment E852 at Brookhaven. Data were
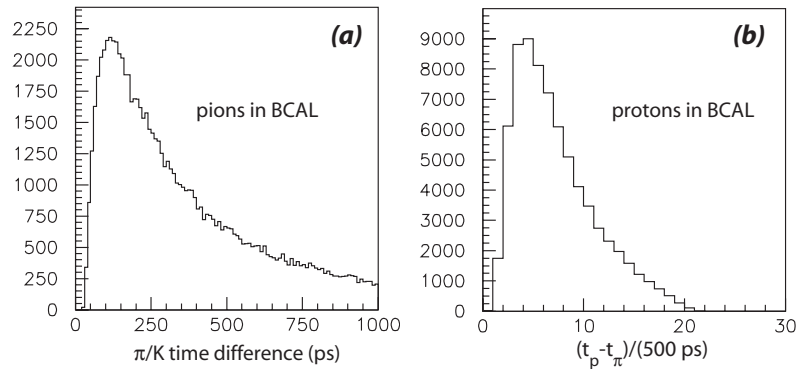
Figure 1.13: (a) The distribution in π/K time difference for $\pi^\pm$ reaching BCAL from the reaction $\gamma p \to \pi^+\pi^+\pi^- p$; (b) For protons reaching BCAL, the proton/pion time difference divided by 500 ps, the assumed mean time resolution for BCAL for minimum ionizing particles.

collected from $\pi^- p$ interactions at 18 GeV/c leading to the final states $\pi^- \pi^0 \pi^0 p$ and $\pi^- \pi^- \pi^+ p$ [30]. That experiment used the multiparticle spectrometer (MPS) at the AGS and utilized a lead glass calorimeter on which the FCAL design is based. Figure 1.14 shows the results of an amplitude analysis for the $J^{PC} = 2^{++}$ and $J^{PC} = 4^{++} \rho\pi$ amplitudes. Two well-established meson states are observed in these amplitudes, the tensor state $a_2(1320)$ in the former and the spin-4 state $a_4(2040)$ in the latter. The intensity of the a_4 is about 3% that of the a_2 and the amplitude of the a_4 is similar for the $\pi^- \pi^0 \pi^0$ and $\pi^- \pi^- \pi^+$ systems, even though the experimental systematics for these two modes are very different.

How do GLUEX and E852 compare? The resolutions obtained for the π^0 mass resolutions for GLUEX calorimetry are similar to those obtained in E852. Studies are underway to estimate the charged particle momentum and angle resolutions. The $\pi^- \pi^- \pi^+$ and $\pi^- \pi^+$ effective mass distributions and distribution in momentum transfer from incoming beam to outgoing 3π system observed in E852 were used to generate a Monte Carlo event sample of a similar final state for 9 GeV photoproduction. Charged particle momenta and angles were smeared using current best-estimate resolution functions and the result was that the resolution in the square of the missing-mass recoiling against the 3π system for GLUEX will be at least as good as that in E852. This would indicate that the ability to kinematically identify exclusive reactions should also be at least as good.

1.10   Conclusions

1. The detection and measurement of π^0 and η mesons with adequate acceptance and resolution is essential for mapping the spectrum of exotic hybrid mesons.

2. Photoproduction at 9 GeV is expected to provide a rich hunting ground for exotic mesons. What little data on photoproduction exists at these energies provides almost no information on final states with multi-neutrals.

3. Fixed target photoproduction imposes a solenoidal geometry for the detector (see Figure 1.1), including cylindrical tracking (CDC) and calorimetry (BCAL) and circular planar tracking (FDC) and calorimetry (FCAL).

4. Calorimeters with requirements similar to BCAL and FCAL have been built and operated. The KLOE
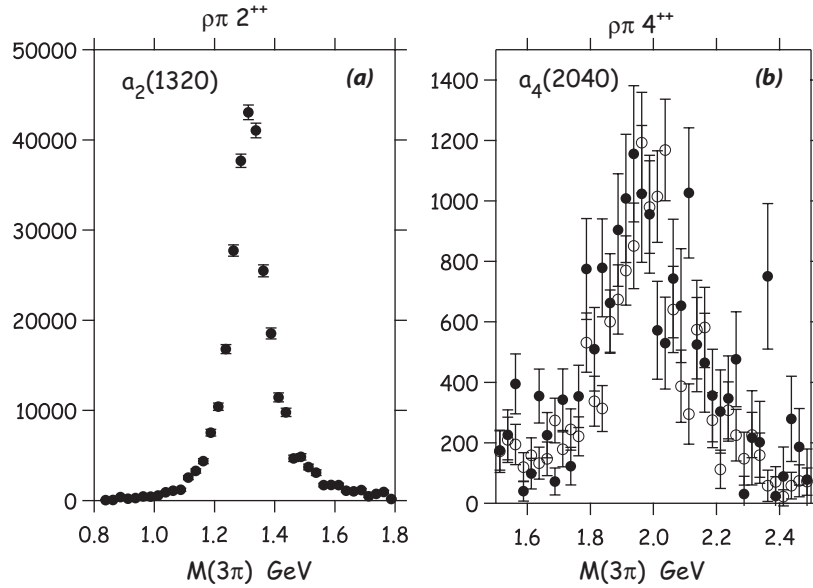
Figure 1.14: (a) Results of an amplitude analysis of data from $\pi^- p$ interactions at 18 GeV/c leading to the final states $\pi^- \pi^0 \pi^0 p$ and $\pi^- \pi^- \pi^+ p$ from Brookhaven experiment E852 [30]. Results are shown for the (a) $J^{PC} = 2^{++}$ and (b) $J^{PC} = 4^{++} \rho\pi$ amplitudes. Filled circles are for the $\pi^- \pi^0 \pi^0$ system and unfilled for the $\pi^- \pi^- \pi^+$ system. In (a) the tensor state $a_2(1320)$ is observed and in (b) the well-established spin-4 $a_4(2040)$ is seen. Note that the intensity of the a_4 is about 3% that of the a_2.

> calorimeter provides guidance for BCAL and the lead glass calorimeter used in E852 and RADPHI provides guidance for FCAL.

5. A version of PYTHIA, tuned to agree with what is known about photoproduction at GLUEX energies, provides us with guidance on the angular and energy spectra of photons illuminating BCAL and FCAL. These studies indicate that the planned coverage and granularity are adequate.

6. Simulations of GLUEX signature reactions leading to final states such as $\eta\pi^0 p$, $b_1\pi p$, ϕp and $3\pi p$ provide guidance on what is required for energy threshold and energy and position resolution for photons.

7. Achievable mean-time resolution for BCAL is adequate for π/p separation but not for π/K separation.

In what follows the design of BCAL and FCAL will be described followed by results of detailed studies of the expected response to a number of GLUEX reactions. Those studies will include GEANT-based simulations of BCAL and FCAL and other features of the GLUEX detector, such as the presence of cabling from tracking chambers and the application of photon reconstruction software followed by kinematic fitting all in the presence of electromagnetic and hadronic backgrounds.

References

[1] M. Adinolfi et al. The KLOE electromagnetic calorimeter. *Nucl. Instrum. Meth.*, A482:364–386, 2002.

[2] M. Adinolfi et al. The KLOE electromagnetic calorimeter. *Nucl. Instrum. Meth.*, A494:326–331, 2002.

[3] B. B. Brabson et al. A study of two prototype lead glass electromagnetic calorimeters. *Nucl. Instrum. Meth.*, A332:419–443, 1993.

[4] R. R. Crittenden et al. A 3000 element lead-glass electromagnetic calorimeter. *Nucl. Instrum. Meth.*, A387:377–394, 1997.

[5] R. T. Jones et al. A bootstrap method for gain calibration and resolution determination of a lead-glass calorimeter. *Nucl. Instrum. Meth.*, A566:366–374, 2006.

[6] R. T. Jones et al. Performance of the RADPHI detector and trigger in a high rate tagged photon beam. *Nucl. Instrum. Meth.*, A570:384–398, 2007.

[7] Gunnar S. Bali et al. Static potentials and glueball masses from QCD simulations with Wilson sea quarks. *Phys. Rev.*, D62:054503, 2000.

[8] Y. Nambu. Technical report, U. of Chicago Report No. 70-70, 1970.

[9] Nathan Isgur and Jack E. Paton. A Flux Tube Model for Hadrons in QCD. *Phys. Rev.*, D31:2910, 1985.

[10] Claude W. Bernard et al. Exotic mesons in quenched lattice QCD. *Phys. Rev.*, D56:7039–7051, 1997.

[11] Thomas D. Cohen. Quantum number exotic hybrid mesons and large N(c) QCD. *Phys. Lett.*, B427:348–352, 1998.

[12] Eberhard Klempt and Alexander Zaitsev. Glueballs, Hybrids, Multiquarks. Experimental facts versus QCD inspired concepts. *Phys. Rept.*, 454:1–202, 2007.

[13] Andrei Afanasev and Philip R. Page. Photo- and electroproduction of $J^{PC} = 1^{-+}$ exotics. *Phys. Rev.*, D57:6771–6777, 1998.

[14] C. McNeile and C. Michael. Decay width of light quark hybrid meson from the lattice. *Phys. Rev.*, D73:074506, 2006.

[15] W.-M. Yao et al. Review of particle physics. *J. Phys.*, G33:1, 2006.

[16] H. H. Bingham et al. Total and partial γp cross sections at 9.3 GeV. *Phys. Rev.*, D8:1277–1286, 1973.

[17] J. Ballam et al. Vector meson production by polarized photons at 2.8, 4.7 and 9.3 GeV. *Phys. Rev.*, D7:3150–3177, 1973.

[18] Y. Eisenberg et al. Photoproduction of ω mesons from 1.2 to 8.2 GeV. *Phys. Lett.*, B34:439–442, 1971.

[19] Y. Eisenberg et al. Study of high energy photoproduction with positron-annihilation radiation. I. Three-prong events. *Phys. Rev.*, D5:15–38, 1972.

[20] G. Alexander et al. Study of high energy photoproduction with positron-annihilation radiation. II. The reaction $\gamma p \to p\pi^+\pi^+\pi^-\pi^-$. *Phys. Rev.*, D8:1965–1978, 1973.

[21] G. Alexander et al. Study of high energy photoproduction with positron-annihilation radiation. III. The reactions $\gamma p \to p2\pi^+2\pi^-\pi^0$ and $\gamma p \to n3\pi^+2\pi^-$. *Phys. Rev.*, D9:644–648, 1974.

[22] T. Sjöstrand, S. Mrenna, and P. Skands. Pythia 6.4 Physics and Manual. Technical report, Lund University, 2006. hep-ph/0603175 and http://www.thep.lu.se/~torbjorn/Pythia.html.

[23] A. Dzierba. Comparing Pythia Simulations with Photoproduction Data at 9 GeV. Technical report, GlueX Document, 2007. GlueX-doc-856-v1.

[24] J. Ballam et al. Energy dependence of the reaction $\gamma p \rightarrow \rho^- \Delta^{++}$. *Phys. Rev.*, 26:995–997, 1971.

[25] N. Kolev et al. Dependence of the spatial and energy resolution of BCAL on segmentation. Technical report, GlueX Document, 2007. GlueX-doc-659-v2.

[26] B. Leverington. Analysis of the BCAL beam tests. Technical report, GlueX Document, 2007. GlueX-doc-804-v4.

[27] R. Lindenbush. A study of the reaction $\pi^- p \rightarrow \eta \pi^0 n$ at 18 GeV/c. Ph. D. Thesis - Indiana University, 1998.

[28] A. R. Dzierba et al. A study of the $\eta \pi^0$ spectrum and search for a $J^{PC} = 1^{-+}$ exotic meson. *Phys. Rev.*, D67:094015, 2003.

[29] D. Lawrence. Track fitting in GlueX: Development Report III. Technical report, GlueX Document, 2007. GlueX-doc-761-v2.

[30] A. R. Dzierba et al. A partial wave analysis of the $\pi^- \pi^- \pi^+$ and $\pi^- \pi^0 \pi^0$ systems and the search for a $J^{PC} = 1^{-+}$ meson. *Phys. Rev.*, D73:072001, 2006.